You may also be interested in:

Nanometrology Using the Transmission Electron Microscope: Imaging
V Stolojan

Zernike phase contrast cryo-electron microscopy reveals 100 kDa component in a protein complex
Yi-Min Wu, Chun-Hsiung Wang, Jen-wei Chang et al.

On the validity of the weak-phase and other approximations in the analysis of electron microscope images
D L Misell

Electron holography—basics and applications
Hannes Lichte and Michael Lehmann

Conventional and scanning transmission electron microscopy: image contrast and radiation damage
D L Misell

An examination of an iterative method for the solution of the phase problem in optics and electron optics: I. Test calculations
D L Misell

New Journal of Physics

The open access journal at the forefront of physics

CrossMark

PAPER

High-resolution transmission electron microscopy with an electrostatic Zach phase plate

S Hettler[1], M Dries[1], J Zeelen[2], M Oster[2], R R Schröder[2] and D Gerthsen[1]

[1] Laboratory for Electron Microscopy, Karlsruhe Institute of Technology, Engesserstr. 7, Karlsruhe, D-76131, Germany
[2] CellNetworks, BioQuant, Heidelberg University, Im Neuenheimer Feld 267, Heidelberg, D-69120, Germany

E-mail: simon.hettler@kit.edu

Keywords: transmission electron microscopy, phase plate, phase contrast, high resolution

Abstract

A new method to control lattice-fringe contrast in high-resolution transmission electron microscopy (HRTEM) images by the implementation of a physical phase plate (PP) is proposed. PPs are commonly used in analogy to Zernike PPs in light microscopy to enhance the phase contrast of weak-phase objects with nm-sized features, which often occur in life science applications. Such objects otherwise require strong defocusing, which leads to a degradation of the instrumental resolution and impedes intuitive image interpretation. The successful application of an electrostatic Zach PP in HRTEM is demonstrated by the investigation of single crystalline Si and Ge samples. The influence of the Zach PP on the image formation process is assessed by analyzing the amplitudes of (111) reflections in power spectra which show a cosine-type dependence on the induced phase shift under certain conditions as predicted by theory.
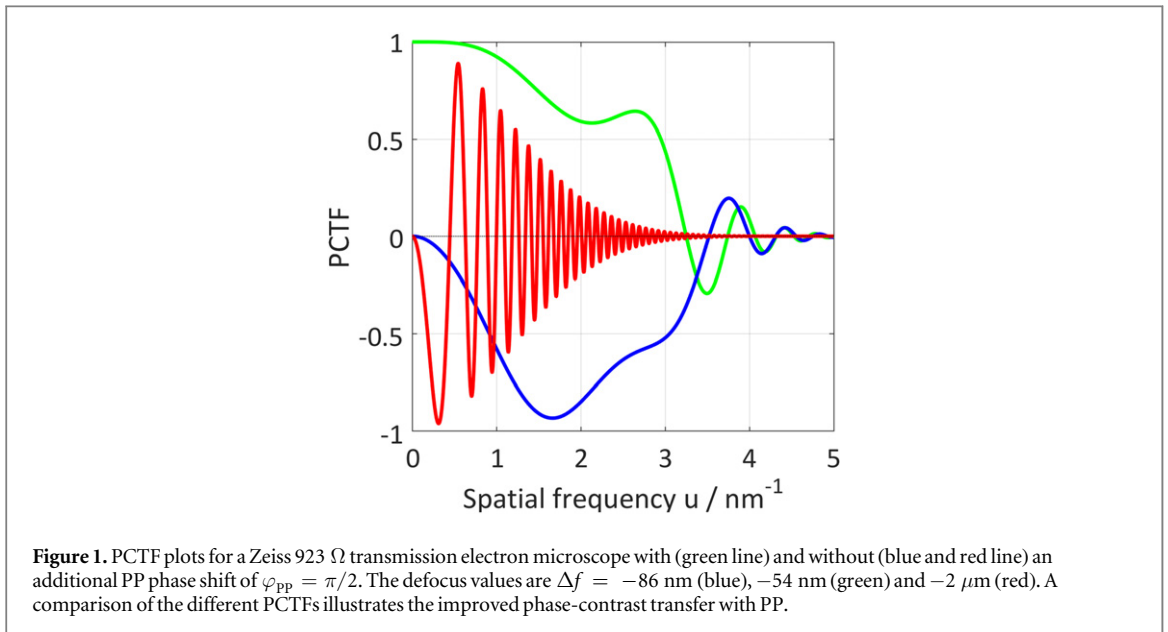
1. Introduction

Transmission electron microscopy (TEM) is routinely applied to obtain images with atomic resolution. In TEM, an electron-transparent specimen is illuminated by a plane electron wave, whose phase and amplitude is altered upon propagation through the object. In the following image formation process, the lens aberrations of the imaging lens system play an important role. The achievable image contrast mainly depends on the structure, thickness and elemental composition of the specimen as well as the chosen imaging parameters.

High-resolution (HR) TEM imaging requires very thin objects, which, depending on their properties, may only weakly modify the phase of the electron wave, while the amplitude remains essentially unchanged. Phase contrast of so-called weak-phase objects (WPOs) is only obtained if an additional phase shift (ideally $\pi/2$) is generated between the scattered and unscattered part of the object wave. In conventional TEM, the lens aberrations of the imaging system are exploited to generate such a phase shift. The phase contrast transfer function (PCTF), which is given by equation (1), describes the transfer of phase information encoded in the object wave below the specimen into image intensity [1]

$$\text{PCTF} \sim \sin\left(\pi/2\left(2\lambda\Delta f u^2 + \lambda^3 C_s u^4 + \varphi_{\text{PP}}\right)\right). \tag{1}$$

The PCTF depends on the spatial frequency u, the electron wave length λ, the spherical aberration coefficient of the objective lens C_s and the defocus value Δf, which must be adapted to the object's spectrum of spatial frequencies to optimize phase contrast. The additional phase shift φ_{PP} is equal to zero in microscopes without a physical phase plate (PP) and will be discussed below. The argument of the sine-function in the PCTF describes the phase shift imposed on the object wave by the aberrations of the imaging lens system. To obtain phase contrast of WPO's, the argument should therefore be close to $\pm\pi/2$ which leads to values of the PCTF near ±1 and thus results in strong contrast transfer.

To achieve optimal contrast in HRTEM imaging, Δf is usually set to Scherzer-defocus Δf_S [2], which partially compensates for the effect of spherical aberration and results in a broad band of spatial frequencies, for which strong phase contrast is observed. The blue line in figure 1 shows the PCTF at $\Delta f_S = -86$ nm for the Zeiss

Figure 1. PCTF plots for a Zeiss 923 Ω transmission electron microscope with (green line) and without (blue and red line) an additional PP phase shift of $\varphi_{PP} = \pi/2$. The defocus values are $\Delta f = -86$ nm (blue), -54 nm (green) and -2 μm (red). A comparison of the different PCTFs illustrates the improved phase-contrast transfer with PP.

923 Ω TEM ($C_s = 2.2$ mm) operated at 200 kV ($\lambda = 2.5$ nm^{-1}), which was used for the experiments in this work. Strong contrast transfer is obtained from $u = 1$ to 3 nm^{-1}. With its first zero at $u = 3.6$ nm^{-1}, the PCTF starts to oscillate. This marks the point resolution of the microscope upon which phase contrast cannot be interpreted directly. It is noted, that the damping of the PCTF towards higher spatial frequencies stems from partial spatial and temporal coherence of the electron wave as detailed in [1].

Due to the sine-type behavior of the PCTF, the transfer of lower spatial frequencies (corresponding to large object features) is weak. Strong contrast transfer of low spatial frequencies requires large Δf values which shift the first maximum of the PCTF towards lower u values as demonstrated by the PCTF plot for $\Delta f = -2$ μm in figure 1 (red line). However, the large Δf value leads to severe degradation of the instrumental resolution and impedes intuitive image interpretation.

The limitations of conventional phase-contrast TEM imaging illustrated above have triggered enormous efforts to develop PPs for TEM which are inspired by Zernike PPs in light microscopy [3] and facilitate in-focus TEM imaging of WPOs. By adding an additional phase shift of $\varphi_{PP} = \pi/2$ between the scattered and unscattered parts of the electron wave, the PCTF (equation (1)) can be turned into a cosine-type function (green line in figure 1). It is obvious that phase contrast is strongly enhanced for low and intermediate spatial frequencies with only a small reduction of the point resolution.

Numerous different PP concepts were proposed [4], since Danev and Nagayama presented the first successful application of a PP in TEM [5]. In most approaches, phase contrast is produced by either placing a thin amorphous carbon film or an electrode in the back focal plane (BFP) of the objective lens which generate the required relative phase shift of $\varphi_{PP} = \pi/2$. The recently developed hole-free PP design, which utilizes an electron-beam induced phase shift caused by the illumination of a thin amorphous carbon film, shows so far the most promising results [6, 7]. However, the underlying physical principles are not yet fully understood. A major drawback of thin-film PPs in general is scattering of electrons in the PP itself which degrades the achievable instrumental resolution.

In contrast, electrostatic PPs [8–13] are not limited by electron scattering and are therefore better suited for HRTEM applications. In addition, the sign and value of the induced phase shift φ_{PP} can be controlled by electrostatic PPs which facilitates contrast optimization not only for WPOs. Furthermore, the variable φ_{PP} allows the reconstruction of the amplitude and phase of the object exit wave function by taking only three images with different φ_{PP} [14].

PP application has been up to now confined to life-science objects like cells, biomolecules or bacteria [15–17]. However, the spatial resolution of the demonstrated PP imaging is still substantially lower than the point resolution of the used electron microscopes.

In this work, we demonstrate for the first time that HRTEM lattice fringe imaging can be achieved with an electrostatic Zach PP using single crystalline Si and Ge samples as test objects. We analyze the amplitudes of (111) reflections and show that their dependence on φ_{PP} agrees with the behavior derived from theory.
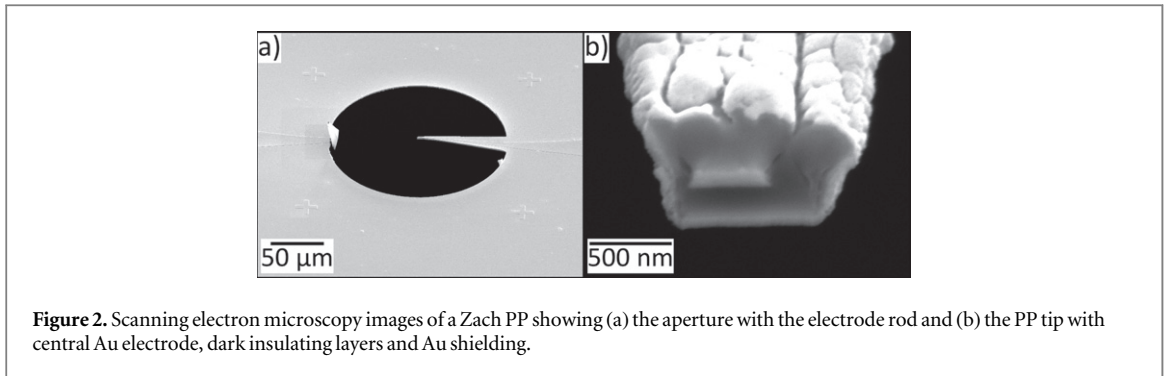
Figure 2. Scanning electron microscopy images of a Zach PP showing (a) the aperture with the electrode rod and (b) the PP tip with central Au electrode, dark insulating layers and Au shielding.
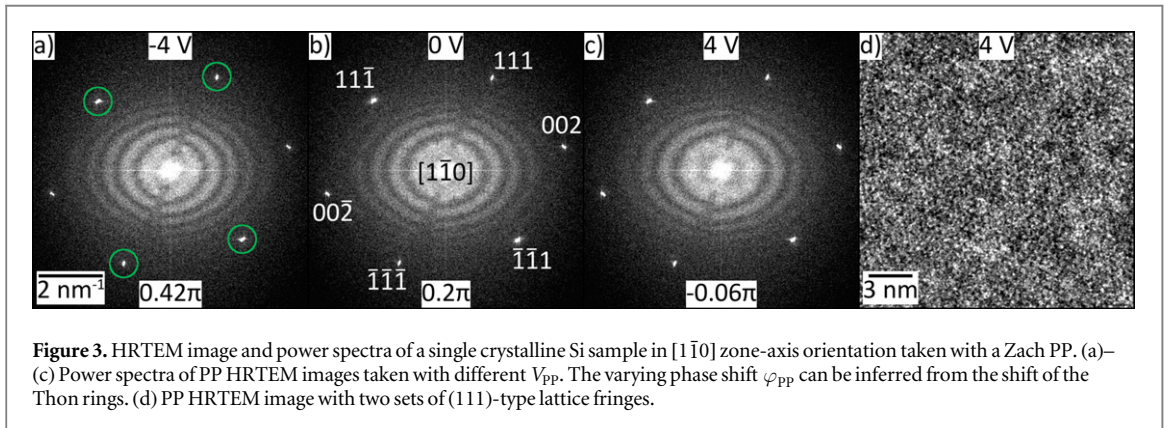

Figure 3. HRTEM image and power spectra of a single crystalline Si sample in $[1\bar{1}0]$ zone-axis orientation taken with a Zach PP. (a)–(c) Power spectra of PP HRTEM images taken with different V_{PP}. The varying phase shift φ_{PP} can be inferred from the shift of the Thon rings. (d) PP HRTEM image with two sets of (111)-type lattice fringes.

2. Methods

Figure 2 depicts scanning electron microscopy images of the Zach PP used for the experiments. The PP acts as an objective aperture with a radius corresponding to 5 nm^{-1} (figure 2(a)). The rod contains an insulated and shielded electrode with an open end (figure 2(b)). The fabrication process is based on a series of different lithography, deposition and etching processes and is described in detail elsewhere [18].

The PP was inserted in the BFP of a Zeiss 923 Ω transmission electron microscope operated at 200 kV with the PP tip positioned close to the zero-order beam (ZOB). A voltage V_{PP} applied to the electrode generates an inhomogeneous electrostatic potential at the PP tip and imposes an adjustable phase shift φ_{PP} on the unscattered part of the electron wave. The sign and value of φ_{PP} is controlled by V_{PP}.

The Zeiss 923 Ω microscope is not optimized for HRTEM. It is characterized by a Scherzer point resolution of 0.28 nm only slightly exceeding the (111)-type lattice plane distances of the Si ($d_{111} = 0.314$ nm) and Ge ($d_{111} = 0.327$ nm) test specimens. The PP aperture permits transmission of spatial frequencies up to $1/0.2$ nm^{-1}.

3. Results and discussion

3.1. Proof of principle

A single crystalline Si sample in $[1\bar{1}0]$ zone-axis orientation was used to demonstrate HRTEM imaging with an electrostatic Zach PP. Figures 2(a)–(c) display three power spectra of a series of PP HRTEM images acquired from the same sample area at a defocus of 260 nm with different V_{PP}. The power spectra reveal the two pairs of (111) reflections marked by green circles in figure 3(a) as well as the (002) reflections and the electrode rod of the Zach PP. Two sets of (111)-type lattice fringes can be recognized in the HRTEM image in figure 3(d).

Including an amorphous part in the illuminated sample area leads to the presence of Thon rings which are exploited to determine φ_{PP} by a pattern recognition process [19] adapted to PP TEM [20]. A relatively large defocus value of 260 nm was chosen in this proof of principle experiment to clearly demonstrate the effect of φ_{PP}, which is visualized by the shift of Thon rings in figures 2(a)–(c). The corresponding φ_{PP} values are 0.42π, 0.2π and -0.06π. Slight charging of the PP leads to a minor elliptic deformation of the Thon rings. Due to distortions induced by the Ω energy filter of the Zeiss 923 Ω microscope, the angles between the individual reflections differ from the expected values.
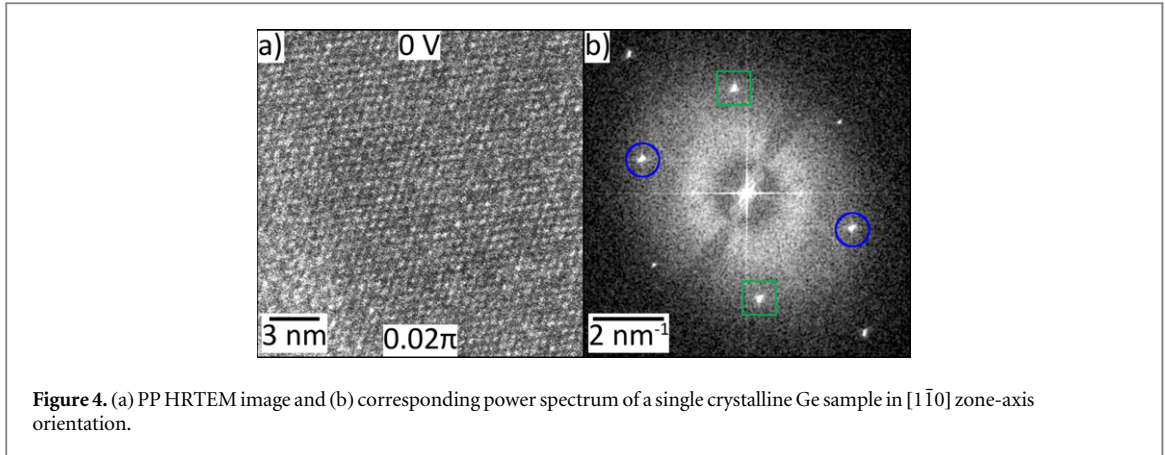
Figure 4. (a) PP HRTEM image and (b) corresponding power spectrum of a single crystalline Ge sample in $[1\bar{1}0]$ zone-axis orientation.

3.2. Image formation with the Zach PP

The influence of the Zach PP on the image formation process is further analyzed by determining the amplitudes of the (111) reflections in power spectra in dependence of φ_{PP}. The functional behavior of this dependence can be derived from imaging theory following the formalism of the transmission cross coefficient (TCC) [21].

The Fourier-transformed image wave function $\tilde{I}_{111}$ at the position of a (111) reflection in a power spectrum for a Si or Ge single crystal in $[1\bar{1}0]$ zone-axis orientation is in general composed of several linear and nonlinear contributions. All Bragg diffracted beams fulfilling $\vec{u} - \vec{u}' = \vec{u}_{111}$ have to be considered which results in four contributions arising from the interference between $\vec{u}_{111}$ and $\vec{u}_0$, $\vec{u}_0$ and $\vec{u}_{\bar{1}\bar{1}\bar{1}}$, $\vec{u}_{002}$ and $\vec{u}_{\bar{1}\bar{1}1}$ as well as $\vec{u}_{11\bar{1}}$ and $\vec{u}_{00\bar{2}}$. Higher-order beams are obstructed by the PP aperture

$$\begin{aligned}
\tilde{I}_{111} = &\ \tilde{\psi}_{111}\tilde{\psi}_0^* \, T(\vec{u}_{111}, \vec{u}_0) + \tilde{\psi}_0\tilde{\psi}_{\bar{1}\bar{1}\bar{1}}^* T(\vec{u}_0, \vec{u}_{\bar{1}\bar{1}\bar{1}}) \\
&+ \tilde{\psi}_{002}\tilde{\psi}_{\bar{1}\bar{1}1}^* T(\vec{u}_{002}, \vec{u}_{\bar{1}\bar{1}1}) \\
&+ \tilde{\psi}_{11\bar{1}}\tilde{\psi}_{00\bar{2}}^* T(\vec{u}_{11\bar{1}}, \vec{u}_{00\bar{2}}).
\end{aligned} \tag{2}$$

$\tilde{\psi}_{\vec{u}} = a_{\vec{u}}e^{i\varphi_{\vec{u}}}$ is the Fourier-transformed object wave function with amplitude $a_{\vec{u}}$ and phase $\varphi_{\vec{u}}$ of the respective beam at the spatial frequency $\vec{u}$. The TCC $T(\vec{u}, \vec{u}')$ depends on the envelope function E taking into account partial temporal and spatial coherence of the electron wave and the wave aberration function χ

$$\begin{aligned}
T(\vec{u}, 0) &= T^*(0, \vec{u}) = E(\vec{u}, 0) \exp(i\chi(\vec{u}) - i\varphi_{PP}) \\
T(\vec{u}, \vec{u}') &= E(\vec{u}, \vec{u}') \exp(i(\chi(\vec{u}) - \chi(\vec{u}'))).
\end{aligned} \tag{3}$$

φ_{PP} is only imposed on the ZOB $\vec{u}_0$ and, hence, only the first and second contribution in equation (2) depend on φ_{PP}. However, in an experiment only the amplitude $A_{111} = |\tilde{I}_{111}|$ of a (111) reflection can be measured. Taking the modulus of the complex image wave function causes an interference between the four complex-valued contributions in equation (2) and leads to a complicated dependence of A_{111} on φ_{PP}. An approximate solution can be calculated by making several assumptions. If the amplitude a_{002} of the $\vec{u}_{002}$ beam, which is forbidden under kinematic conditions, is small compared to the amplitude a_0 of the ZOB $\vec{u}_0$, equation (2) can be reduced to the first and second term. The validity of this assumption is checked by calculating the amplitudes and phases of the corresponding beams for Si and Ge using the STEMsim software [22]. For Si, the assumption is only correct for thin samples with a thickness below 15 nm, whereas it holds true for Ge samples with larger thicknesses. The amplitude A_{111} can be easily calculated if a perfect zone-axis orientation ($a_{\vec{u}} = a_{-\vec{u}}$, $\varphi_{\vec{u}} = \varphi_{-\vec{u}}$) and an isotropic envelope and wave aberration function is assumed

$$A_{111} \sim a_0 a_{111} E(\vec{u}_{111}, 0) \, |\cos(\Theta - \varphi_{PP})|. \tag{4}$$

The angle $\Theta = \varphi_{111} - \varphi_0 + \chi(\vec{u}_{111})$ is a phase offset which is not dependent on φ_{PP}. A_{111} determined from power spectra of HRTEM images is therefore expected to oscillate with φ_{PP}.

Figure 4 shows a HRTEM image of a single crystalline Ge sample in $[1\bar{1}0]$ zone-axis orientation acquired with a Zach PP. The measured defocus value of -94 nm is close to Scherzer conditions (-86 nm). The HRTEM image (figure 4(a)) and the power spectrum (figure 4(b)) are part of an image series acquired with different V_{PP}. The corresponding φ_{PP} values were determined for each image by a pattern recognition process [20].

A_{111} is determined for the two pairs of (111) reflections marked by green boxes and blue circles in figure 4(a) for every image of the series. The result is plotted in figure 5 (green boxes and blue circles) as a function of φ_{PP}. The experimental data is fitted by a function with the expected dependence given by equation (4) (blue and green lines in figure 5). The data agrees well with the fit but the curves do not coincide.
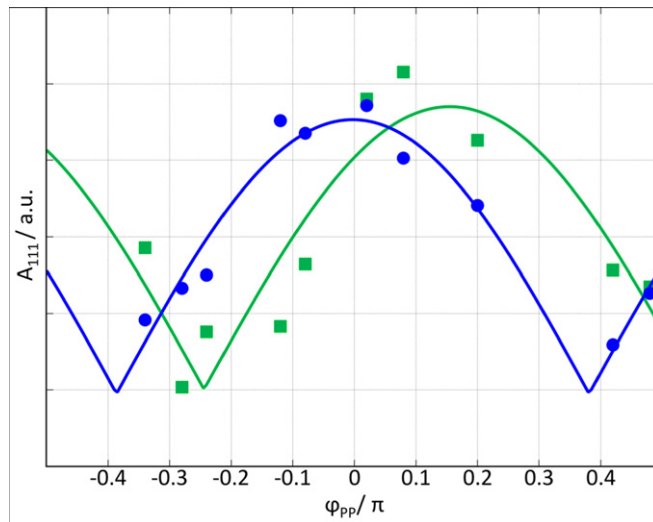
Figure 5. Plot of the amplitude of the Ge (111) reflection pairs marked green and blue in figure 4(b) from the image series acquired with varying φ_{PP} from -0.4π to 0.5π.

Several reasons can lead to the difference between the individual A_{111}. The oscillation amplitude is given by the envelope function E and the amplitudes a_0 and a_{111} (equation (4)). A slight tilt from perfect zone-axis orientation or an anisotropic envelope function E can be responsible for the small difference in amplitude between the green and blue curve in figure 5. The second observed difference is the displacement of the curves against each other. This shift is caused by different phase offsets Θ which originate again from either an imperfect zone-axis orientation or an anisotropic wave aberration function χ. The fact that both differences are relatively small in figure 5 suggests that the PP does not introduce additional distortions except the slight astigmatism visible in figure 4.

An instructive experiment is depicted in figure 6. It shows a PP HRTEM image of a Si single crystal in $[1\bar{1}0]$ zone-axis orientation (figure 6(a)). In this particular case, the PP rod partially blocks one pair of (111) reflections in the BFP (red circles in figure 6(b)). This leads to a strong reduction of the amplitude of the red reflection pair and the HRTEM image only shows one set of lattice fringes (figure 6(a)). A_{111} is determined for the two pairs of (111) reflections from a series of PP HRTEM images taken with different V_{PP} and is plotted in figure 6(c).

The obstruction of a red reflection has an influence on the dependence of A_{111} on φ_{PP} for both the red and the green reflection pairs. For the red reflection pair, the obstruction of a red reflection is equivalent to the elimination of the first or second term in equation (2). A change of φ_{PP} then only affects the phase of $\tilde{I}_{111}$, but A_{111} remains unchanged. An oscillatory behavior is therefore not found for the red reflection pair (red circles in figure 6(c)). Additionally, the amplitude is strongly decreased.

For the unaffected green reflection pair (green boxes in figure 6(b)) the obstruction of a red reflection implies the elimination of the third or fourth term in equation (2). Hence, the influence of the (002) beam on A_{111} is reduced and equation (4) remains valid for thicker Si samples. As a result, A_{111} of the green reflection pair shows a cosine-type dependence on V_{PP} (green boxes and line in figure 6(c)).

3.3. Practical considerations

A_{111} should in fact be analyzed as a function of φ_{PP} and not V_{PP} in figure 6(c). However, φ_{PP} was difficult to determine in the corresponding power spectra due to the lack of Thon rings and the presence of minor distortions introduced by the PP. Analyzing the reflection intensities as a function of V_{PP} is still valid if a linear dependence between φ_{PP} and V_{PP} exists.

The linearity is demonstrated in figure 7, where ϕ_{PP} is plotted over V_{PP} for three different distances between the PP tip and the ZOB. The data can be well fitted by straight lines and the gradient yields φ_{PP}/V_{PP}. As the electrostatic potential drops with increasing distance to the PP tip, the ratio φ_{PP}/V_{PP} and thus the gradient decreases for larger distances.

The choice of an appropriate distance between PP tip and ZOB is crucial for a successful application and depends on the objects to be investigated. For typical WPOs in life sciences with feature sizes larger than a few nm, the achievable cut-on frequency of the PP is the limiting factor and the PP must be positioned very close to the ZOB [23]. However, for HRTEM applications and feature sizes below 1–2 nm, the cut-on frequency only plays a minor role. Hence, the distance between PP and ZOB can be enlarged which minimizes contamination
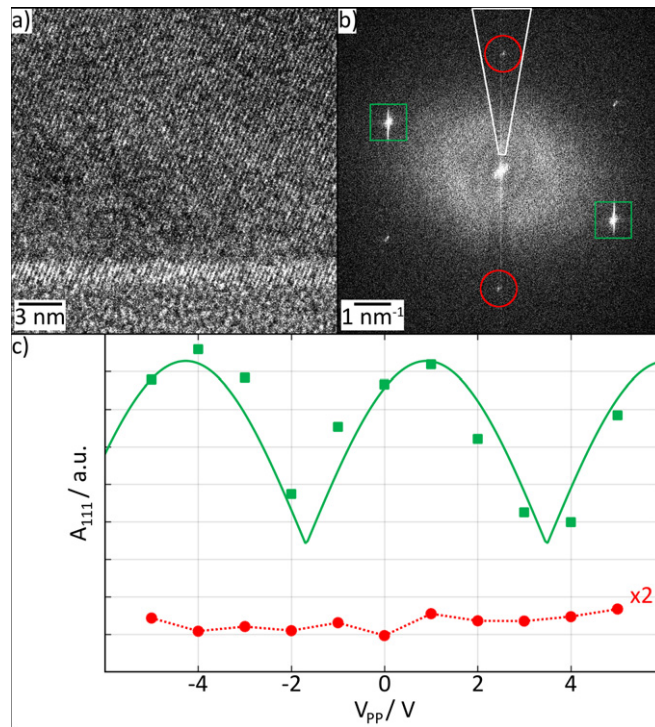
Figure 6. (a) Lattice fringe image of a single crystalline Si sample in [1$\bar{1}$0] zone-axis orientation taken with a Zach PP and (b) corresponding power spectrum. The reflection pair marked red in (b) is partially obstructed by the PP rod. (c) Amplitude of the (111) reflection pairs marked green and red in (b) as a function of V_{PP}.
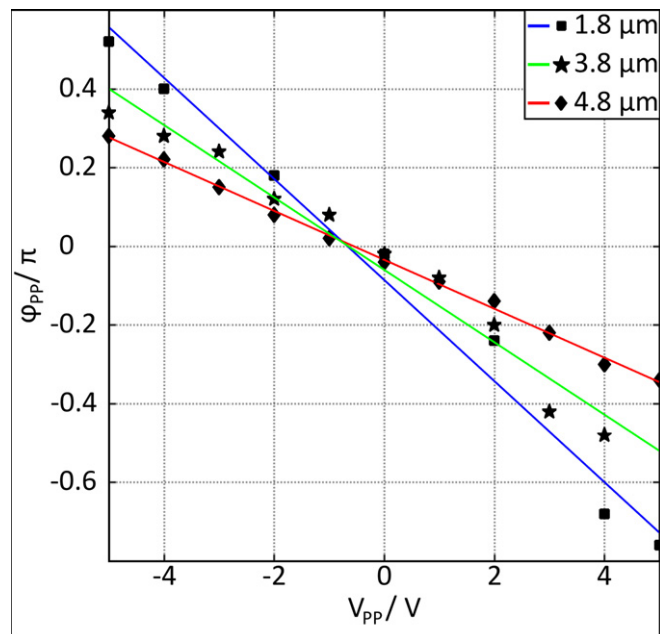

Figure 7. φ_{PP} as a function of V_{PP} for three different distances between the PP tip and the ZOB.

and charging of the PP. Charging of the Zach PP was in fact negligible in the shown experimental results which is demonstrated by the small amount of φ_{PP} induced at $V_{PP} = 0$ V (figure 7).

Moreover, a larger distance between PP tip and ZOB is favorable, because the ZOB is located in a region, where the inhomogeneity of the electrostatic potential is strongly reduced. A possible phase-contrast reduction due to a phase shift gradient over the spatially spread ZOB is minimized [11].

4. Conclusions

The use of PPs in TEM is promising for the generation of phase contrast. However, PP applications were up to now limited to life-science objects and focused on the enhancement of phase-contrast transfer at low spatial frequencies. In this work we have demonstrated that the application of a PP is also promising in lattice (fringe) imaging, because the phase shift imposed by the PP can be utilized as a new parameter to tune HRTEM contrast. We analyzed single-crystalline Si and Ge samples with an electrostatic Zach PP. The experimental results agree well with theory as demonstrated by the oscillation of the amplitude A_{111} of (111) reflections in dependence of the phase shift φ_{PP} (figure 5) or the applied voltage V_{PP}, respectively (figure 6(c)). We could not detect an obvious PP-induced degradation of the instrumental resolution.

The application of PPs in the field of HRTEM is interesting from a general point of view. Installing a PP in an aberration-corrected transmission electron microscope leads to close-to-ideal HRTEM imaging conditions. The PCTF is converted from a sine-type into a cosine-type function and the formation of phase contrast is only limited by the effect of partial coherence of the electron wave [24]. This will improve phase-contrast transfer not only at intermediate and high spatial frequencies but also at low spatial frequencies. In contrast to thin-film PPs, electron scattering in the PP and thus reduction of the coherence of the electron wave is avoided with the electrostatic Zach PP. The ability to choose sign and amount of φ_{PP} suggests that Zach PPs are particularly suited for HRTEM, because quantitative measurements become accessible, e.g. by comparing experimental data with simulations or by applying an object-wave reconstruction process [14].

Acknowledgments

References

[1] Spence J 2013 *High-Resolution Electron Microscopy* 4th edn (Oxford: Oxford University Press)
[2] Scherzer O 1949 *J. Appl. Phys.* **20** 20–9
[3] Zernike F 1942 *Physica* **9** 686–98
[4] Glaeser R M 2013 *Rev. Sci. Instrum.* **84** 111101
[5] Danev R and Nagayama K 2001 *Ultramicroscopy* **88** 243–52
[6] Malac M, Beleggia M, Kawasaki M, Li P and Egerton R F 2012 *Ultramicroscopy* **118** 77–89
[7] Danev R, Buijsse B, Khoshouei M, Plitzko J M and Baumeister W 2014 *Proc. Natl Acad. Sci.* **111** 15635–40
[8] Schultheiss K, Pérez-Willard F, Barton B, Gerthsen D and Schröder R R 2006 *Rev. Sci. Instrum.* **77** 033701
[9] Cambie R, Downing K H, Typke D, Glaeser R M and Jin J 2007 *Ultramicroscopy* **107** 329–39
[10] Shiue J *et al* 2009 *J. Electron Microsc.* **58** 137–45
[11] Schultheiss K, Zach J, Gamm B, Dries M, Frindt N, Schröder R R and Gerthsen D 2010 *Microsc. Microanal.* **16** 785–94
[12] Alloyeau D, Hsieh W K, Anderson E H, Hilken L, Benner G, Meng X, Chen F R and Kisielowski C 2010 *Ultramicroscopy* **110** 563–70
[13] Barton B *et al* 2011 *Ultramicroscopy* **111** 1696–705
[14] Gamm B, Dries M, Schultheiss K, Blank H, Rosenauer A, Schröder R R and Gerthsen D 2010 *Ultramicroscopy* **110** 807–14
[15] Dai W, Fu C, Khant H A, Ludtke S J, Schmid M F and Chiu W 2014 *Nat. Protocols* **9** 2630–42
[16] Fukuda Y, Laugks U, Lučić V, Baumeister W and Danev R 2015 *J. Struct. Biol.* **190** 143–54
[17] Asano S, Fukuda Y, Beck F, Aufderheide A, Förster F, Danev R and Baumeister W 2015 *Science* **347** 439–42
[18] Hettler S, Gamm B, Dries M, Frindt N, Schröder R R and Gerthsen D 2012 *Microsc. Microanal.* **18** 1010–5
[19] Barthel J and Thust A 2010 *Ultramicroscopy* **111** 27–46
[20] Hettler S, Wagner J, Dries M, Oster M, Wacker C, Schröder R R and Gerthsen D 2015 *Ultramicroscopy* **155** 27–41
[21] Ishizuka K 1980 *Ultramicroscopy* **5** 55–65
[22] Rosenauer A and Schowalter M 2007 *Springer Proc. Phys.* **120** 169–72
[23] Frindt N, Oster M, Hettler S, Gamm B, Dieterle L, Kowalsky W, Gerthsen D and Schröder R R 2014 *Microsc. Microanal.* **20** 175–83
[24] Gamm B, Schultheiss K, Gerthsen D and Schröder R R 2008 *Ultramicroscopy* **108** 878–84